Supporting Information for

Direct observations of a three million cubic meter rock-slope collapse with almost immediate initiation of ensuing debris flows

*Fabian Walter1), Florian Amann2), Andrew Kos3), Robert Kenner4) Marcia Phillips4), Antoine de Preux5), Matthias Huss1,6), Christian Tognacca7), John Clinton8), Tobias Diehl8), Yves Bonanomi9)

[1] Laboratory of Hydraulics, Hydrology and Glaciology (VAW), ETH Zurich, Zurich, Switzerland
[2] Chair of Engineering Geology and Hydrogeology, RWTH Aachen University, Germany
[3] Terrasense Switzerland Ltd, Buchs SG, Switzerland
[4] WSL Institute for Snow and Avalanche Research SLF, Davos, Switzerland
[5] Marti AG, Bern, Switzerland
[6] Department of Geosciences, University of Fribourg, Fribourg, Switzerland
[7] Beffa Tognacca Gmbh, Switzerland
[8] Swiss Seismological Service, ETH Zurich, Zurich, Switzerland
[9] Bonanomi AG, Igis, Switzerland

Content of this file

Video S1
Text S1 to S9
Table S1 to S2
Figures S1 to S7

Additional Supporting Information (Files uploaded separately)

Video S1 (Reto Salis, Sciora mountain hut) showing the collapse of the Pizzo Cengalo rock wall on August 23 2017.

Introduction

Text S1 describes the data and observations used to reconstruct the timeline of events. Texts S2 to S4 describe the remote sensing methods. Text S5 describes the kinematic analysis. Text S6 provides supporting information and the methodology to assess the impact of the rock avalanche event on the glacier. Text S7 gives an overview how the velocity of the ice jet was estimated. Text S8 provides details of the low-frequency seismic inversion and Text S9 describes a spectral analysis of the high frequency signal. Table S1 contains a detailed timeline of events. Table S2 provides the seismic velocity model used for the inversion of the rock avalanche's force history. Figures S1 to S7 provide supporting material for the text in this supplementary document.

Text S1: Timeline of rock avalanche and debris flow observation

Available data and observations (e.g. seismic data, photographs / videos, personal observations, eyewitness reports) were used to reconstruct the timeline of the rock avalanche and the subsequent debris flows. The time line is shown in Table S1. An overview map and topographic cross section showing the limits of the 2011 and 2017 rock avalanches, the limits of the debris flows and reference locations mentioned in the timeline are shown in Figure 1 of the main text.

Text S2: Terrestrial Laser Scanning

Terrestrial laser scanning (TLS) was used to acquire 3D point clouds representing the rock slope surface of Pizzo Cengalo. The data were used to quantify the volume of rock fall events and compared with slope deformation measurements acquired with the terrestrial radar interferometer (TRI, see Text S3). Starting in 2013 six measurement campaigns were undertaken between 2012 and 2017 from the ridge of the Bondasca moraine (Figure 1) using a Riegl VZ6000 long-range terrestrial laser scanner. Within the deformation area, the resulting point clouds had a resolution better than 50 cm. The individual point clouds were aligned using the iterative closest point algorithm (Chen and Medioni, 1991). Deformation and volume changes were calculated based on gridded surface elevation models in a slope parallel projection.

Text S3: Portable radar interferometry

A portable terrestrial radar interferometer (TRI) was used to measure rock slope deformations on a yearly basis. The instrument is a frequency modulated continuous wave (FMCW) real aperture radar, with a central frequency of 17.2 GHz (Ku band). The radar utilizes a fan-beam antenna array that rotates around a central axis with sampling rates of up to 10 deg s^{-1}, ensuring very high phase coherence during image acquisition. Movement is measured along the radar line of sight (LOS), with a precision of < 2.0 mm (Wiesmann et al. 2008, Werner et al. 2008, and Werner et al 2012).

A permanent measurement platform was installed on the Bondasca moraine (Figure 1), around 1 km NE of the Pizzo Cengalo NE face. Seven measurement campaigns were undertaken between 2012 and 2017 (Figure 3). Each campaign lasted 3 to 4 hours. Processing of radar data was undertaken using the Gamma software package. Complex radar images from each of the yearly campaigns were stacked to create a single averaged image, corresponding to each of the measurement campaigns. The stacked images were then used to calculate single interferograms. Noise reduction to improve the signal to noise ratio was performed using a bandpass filter on the single interferograms. This was followed by linearly normalized atmospheric filtering relative to a phase reference center (e.g. considered stable over the interval being considered). After removal of atmospheric noise, the resultant interferograms were projected within a 3D photogrammetric model. Displacement maps were phase unwrapped and converted to radar line-of-sight. Line-of-sight-displacement rates were calculated by stacking and normalizing single displacement maps. Resultant displacement maps were then projected within a 3D photogrammetric model for visualization. The 3D model used for data visualization was constructed using photogrammetry from unmanned aerial vehicle acquisitions.

Text S4: Airborne laser scanning and orthophoto analysis

Digital elevation models (DEMs) of Val Bondasca are available from regularly taken aerial images using the Airborne Digital Sensor (ADS) by the Swiss Topographic Service (swisstopo) and airborne laser scans after the rock avalanche events 2011 and 2017. Differences between these DEMs reveal the erosion and deposition areas of the rock avalanches released from Pizzo Cengalo. Three DEM differences are used: 1. DEM on 25 August 2017 – corrected baseline DEM from year 2015; 2. DEM on 30 August 2017 – DEM on 25 August 2017; 3. DEM on 05 September 2017 – DEM on 30 August 2017. The resolution of the image strips is between 10 and 12 cm for the scans carried out in 2017 and 50 cm for the image strip scanned in 2015. The resulting DEM had a resolution of 1 m in 2017 and 2 m in 2015. The accuracy is expected to be better than 1 m. Orthofotos, hillshades and topographic maps in the background of Figure 1 are reproduced with the permission of Swisstopo: pixmaps© 2018 swisstopo (5704 000 000), swissimage© 2018, swisstopo (DV 033594).

Text S5: Structural data acquisition and kinematic analysis

Geological structures were mapped using terrestrial photogrammetric data and TLS data. A rangefinder binocular (Vectronix Vector IV) connected to a GPS station (Leica Zeno 15) was used to determine reference points within and in close vicinity to the rock slopes for the photogrammetric analysis. To determine the geometry of structures (i.e. dip and dip direction) the software ShapeMetrix3D (3G Software & Measurement GmbH) was used. Digital elevation models established from TLS data were analysed in terms of structure orientations using the software Coltop3D.

Stereographic analysis techniques applied to our structural data were used to assess the kinematics of the rock slope (Figure S1). This method assumes that all discontinuities are dry, fully persistent, cohesionless, and the blocks are considered rigid. Lateral constraints and external forces on the blocks are not considered. For a given slope angle and orientation of discontinuity set the analysis indicates potential kinematic modes. It was assumed that toppling is only possible when the poles of discontinuities controlling toppling have azimuths deviating less than 30° from the slope dip direction (Goodman, 1989). It was further assumed that toppling is only possible when the ratio of the rock column base length to the height does not exceed the tangent of the dip angle (Goodman and Bray, 1976). For the sliding analysis, an envelope deviating 20° from the slope dip direction was assumed (Wyllie and Mah, 2004). Wedge sliding is considered possible if the intersection line of two planes dip at an angle lower than the slope angle and greater than the friction angle (Markland, 1972). A friction angle of 35° was assumed. Toppling, planar sliding, and wedge sliding were analysed for an overall slope orientation of 75°/70°.

Text S6: Glacier impact and ice erosion

The nameless glacier below Pizzo Cengalo had an area of about 0.16 km^2 by the year 2009 and an estimated total volume of roughly 4 $\times 10^6$ m^3. The glacier was steep and highly crevassed in its upper part, and covered with debris in its lower reaches. Extreme winter accumulation rates due to avalanching in the cirque, which is surrounded by 500-1000 m high rock faces, and limited solar radiation due to a northerly exposure contribute to a comparably low elevation of the glacier (2080-2640 m a.s.l.). For assessing glacier evolution and mass balance over the last decades a series of DEMs based on aerial photogrammetry was available (1991, 2003, 2009, 2012, 2015, 2017, Table 1). By differencing the DEMs, glacier elevation and volume changes were evaluated. Changes in surface elevation over the glacier can be due to (i) snow accumulation or snow/ice melt driven by meteorological variables, (ii) erosion and deposition of sediments on the ice surface, and (iii) ice erosion due to direct impact of rock falls.

The very small glacier below Pizzo Cengalo showed thickness changes of approximately –1 m a^{-1} on average over the last decades, typical for Alpine glaciers. The rock fall event of 2011 only had a minor impact on the glacier and the eroded ice volume was likely $<0.1\times10^6$ m^3. For quantifying the impact of the major 2017 event, we compared the DEMs from August 30, 2015 and August 27, 2017, acquired four days after the 2017 rock fall event (Figure S3). The net volume change over the glacier-covered surface was found to be -0.75×10^6 m^3. Accounting for glacier mass loss due to melting prior to the event, as well as deposition of sediments in the lower reaches of the glacier before or during the landslide, we determined a total eroded ice volume of $0.6 \pm 0.1\times10^6$ m^3 as a direct consequence of the failure event on August 23, 2017. Local ice thickness losses were as high as 20 m. Most of the ice was eroded in the cirque, i.e. in the direct impact zone of the rock mass, whereas the lower part of the glacier was only barely affected (Figure S2). Over about half of its previous area, the glacier was completely removed, exposing the bedrock.

Text S7: Estimation of ice-jet velocity

The catastrophic rock wall collapse on 23 August 2017 was captured on video (supplementary material). The footage was used to establish a first order approximation of the velocity of the leading edge of the ice-jet that was ejected in association with the rock fall impact on the glacier at the toe of Pizzo Cengalo (Figure 1). The duration the ice-jet was airborne was timed from the video. The approximate distance from the W-face of the Bügeleisen ridge, where the ice-jet trajectory was deviated towards the north, and the fall out point of the leading edge of the ice-jet were estimated in several steps: 1) the fall out time was determined in the video, 2) the fall-out location visible from the Sciora hut was collated in line of sight to a point in the Pizzo Badile North-face 3) this trajectory was transferred into an aerial photograph, 4) the ice-jet trajectory was assumed to be parallel to the W-face of the Bügeleisen ridgeline, 5) the two trajectories give a first order approximation of the distance the ice-jet was airborne.

Text S8: Inversion of Low-Frequency Seismograms

The net forces, which act during acceleration and deceleration phases of the rock avalanche's bulk mass induce low- frequency surface waves sometimes detectable at thousands of kilometer distances [e.g. Allstadt et al., 2018]. This includes the initial elastic rebound of the mountain massif upon the detachment of the rock avalanche mass. In the frequency domain, the Earth's elastic displacement U(x,ω) at point x in response to the rock avalanche's force history F(ω) can be expressed as

$$U_i(x,\omega)=G_{ij}(x, \omega) \times F_j(\omega). \qquad (1)$$

Subscripts denote geographical directions, '×' represents algebraic multiplication, ω is frequency and summation over repeated indices is assumed. $G_{ij}(x, \omega)$ is the elastic displacement in the i^{th} direction due to a force in the j^{th} direction ("Green's Functions"), which we calculate with the propagator matrix method (Zhu and Rivera, 2002) using a regional 1D seismic velocity model (Tabel S2).

Following a standard approach (for details we refer the reader to Allstadt, 2013; Allstadt et al., 2018, and references therein) we invert the linear equation (1) for each frequency separately using a least squares approach. We use frequencies between 0.006 and 0.1 Hz depending on the signal-to-noise ratio of each station and 400 s time windows with 4000 samples (10 Hz sampling frequency). Centered on the ca. 120 s long-period rock avalanche signals, these time windows include substantial amount of signal-free records from all stations to stabilize the inversion. The entire 400 s seismogram is subjected to a cosine taper to suppress amplitudes near the edges. Most waveform portions are fit satisfactorily at all ten stations shown in Figure S5. An inverse Fourier transform applied to the resulting complex spectra yields the three components of the rock avalanche's force history (Figure 6).

Under the point mass assumption and by Newton's Third law, the negated force history (Figure 6) of the rock avalanche can be used to quantify the trajectory the rock avalanche's mass (Ekström and Stark, 2013). We multiply the density of near-surface crustal material of 2.60 g cm^{-3} [*Stein and Wysession, 2003*] by the rock avalanche volume of 3.5×10^{6} m^{3} (approximate rock and enclosed glacier volume) to obtain a bulk mass estimate by which we divide the force history to obtain the mass acceleration. Single and double integration with respect to time yields an estimate of the rock avalanche's velocity and displacement trajectory, respectively. Assigning its start to the Pizzo Cengalo source region, the trajectory is determined under the assumption that the rock avalanche displacement is small compared to the smallest source-station spacing (Figure S4).

The exact shape of the calculated trajectory depends on the chosen frequency bands and station records. Such numerical instability is well known and may be mitigated by imposing constraints such as stationarity of the avalanche's bulk momentum (Ekström and Stark, 2013). However, in the Pizzo Cengalo case we are interested in dynamic details such as multiple acceleration phases resulting from topographic steps, which would likely be masked by simplifying assumptions about the force history. To obtain an impression for inversion stability, we calculate 100 jackknife force histories, for which we randomly remove the data from two stations and replace them by copies of two other randomly chosen stations. This provides a rough uncertainty estimate for force histories, speeds and trajectories (Figures 6 and S6). The mean of these jackknife force histories is used to calculate the trajectory shown in Figure 7 of the main text. Figure S6 shows this trajectory along with all jackknife trajectories. The standard deviation of the jackknife force histories are subsequently used to estimate uncertainty of the avalanche's along-trajectory speed shown in Figure 6.

Since we invert all frequencies separately, the single force history contains no information about absolute time and we manually pick the onset and end of the force history setting it to zero beyond (Figure 7). In order to assign an absolute time to the force history we align it with the long-period record of the closest station VDL (Figures 5, 6 and S4). We assume that at 24 km distance, this station is close enough to record quasi static elastic displacements, which closely resemble the inverted force history (Figure 6).

The presented seismic inversion describes the motion of the rock avalanche's center of mass assuming a constant rock mass. Dynamic details such as erosion and deposition could be captured by combining the analysis with a granular flow model (e.g. Yamada et al., 2018), which is however beyond the scope of the present study. At this point we rely on interpretation of differences in digital elevation models (DEM's) obtained before and after the event (Figure 2).

Text S9: Analysis of High-Frequency Seismograms

The spectrogram of the 2017 event includes a signature of the rock avalanche and the ensuing first debris flow (Figure S7 and Figure 5 in the main text). We investigate the two signals more closely by calculating spectra for 10 second long time windows during the rock avalanche, during the ensuing debris flow, during the ca. 30 second long time window in between ("Delay") as well as during a pre-event noise window (Figure S7). From the spectrogram appearance, we separate the high-frequency spectra into a <10 Hz band, which includes the maximum energy of the rock avalanche and the 15-30 Hz band, which includes relatively high frequencies of the debris flow signal.

Figure S7C shows the spectra normalized with respect to the maximum, which for all time windows lies well below 10 Hz. For these normalized spectra, the energy levels in the 15-30 Hz range are representative of the relative power between the <10 Hz and the 15-30 Hz ranges. Except for the rock avalanche section, all shown signal and noise-based spectra feature a minimum around 16 Hz. This suggests a path or site effect, meaning that the spectral minimum is not related to source characteristics but rather the propagation of seismic waves from source to the recording station. Only the rock avalanche transmits enough seismic energy to fill this spectral trough.

At all three analyzed time windows (green, cyan and yellow lines in Figures S7A and S7C), the relative debris flow spectra have elevated 15-30 Hz energy distinguishing the debris flow signal from the rock avalanche seismogram (blue lines in Figures S7A and S7C) and the signal in the ca. 30 second long delay (red line in Figures S7A and S7C). This points out that the flow physics during the debris flow is different from the rock avalanche.

Although our choice of separating the high-frequency spectrum into the <10 Hz and 15-30 Hz bands is somewhat arbitrary, we argue that it reflects two regimes of wet granular flows, in our case the rock avalanche and the first debris flow. In such a mixture, high-frequency seismicity can be generated by particle impacts with the bed (Tsai et al., 2012; Lai et al., 2018; Farin et al., 2019) and water turbulence (Gimbert et al., 2014). The peak frequencies of the seismic signal associated with these two processes depend on source-station distance and typically unknown properties of the ground substrate. In general, however, water turbulence tends to generate lower peak frequencies than particle impacts on the ground (Gimbert et al., 2014).

This contrasts with our observation, that for the debris flow, which we expect to involve a water-saturated sediment mixture, the 15-30 Hz frequency band has a relatively higher energy than the rock avalanche. Arguably, the sediment sorting mechanisms in a debris flow give rise to different seismic spectra generated by different portions of the flow (Farin et al., 2019). This may amplify the *relative* spectral power of the particle collisions with the ground.

Given uncertainties in particle sizes, elastic as well as anelastic properties of the ground substrate between Piz Cengalo and the recording station VDL (Figure 5), we refrain from a more quantitative analysis of the high-frequency spectrum. Furthermore, the relative spectral power in the <10 Hz and 15-30 Hz frequency ranges cannot be simply explained by seismogenic particle impacts versus water turbulence. However, we draw the qualitative conclusion that the relative spectral power in the <10 Hz and 15-30 Hz frequency ranges distinguishes the debris flow signal from the rock avalanche. The same is true for the comparison between the debris flow and the ca. 30 second delay indicating that during the delay seismicity generation did not simply fade but a change in or suppression of a flow process took place. This justifies treating the first debris flow as a separate granular flow process.

References

Allstadt, K. (2013). Extracting source characteristics and dynamics of the August 2010 Mount Meager landslide from broadband seismograms. Journal of Geophysical Research: Earth Surface, 118(3), 1472-1490.

Allstadt, K. E., Matoza, R. S., Lockhart, A., Moran, S. C., Caplan-Auerbach, J., Haney, M., Thelen, W. A. & Malone, S. D. (2018). Seismic and acoustic signatures of surficial mass movements at volcanoes. Journal of Volcanology and Geothermal Research.

Chen Y, Medioni G. 1991. Object modeling by registration of multiple range images. In, Robotics and Automation, 1991. Proceedings, 1991 IEEE International Conference on, 2724-2729 vol.3. doi: 10.1109/ROBOT.1991.132043

Ekström, G., & Stark, C. P. (2013). Simple scaling of catastrophic landslide dynamics. Science, 339(6126), 1416-1419.

Farin, M., Tsai, V. C., Lamb, M. P., & Allstadt, K. E. (2019). A physical model of the high-frequency seismic signal generated by debris flows. Earth Surface Processes and Landforms.

Gimbert, F., Tsai, V. C., & Lamb, M. P. (2014). A physical model for seismic noise generation by turbulent flow in rivers. Journal of Geophysical Research: Earth Surface, 119(10), 2209-2238.

Goodman, R. E. (1989): Introduction to Rock Mechanics. 2nd Edition (New York, Wiley, 1989).

Goodman, R.E., Bray, W. J. (1976): Toppling of rock slopes. Proceeding of the Specialty Conference on Rock Engineering in Foundations and Slopes, ASCE, Boulder, Colorado, August 15-18 (1976).

Markland, J. T. (1972): A useful technique for estimating the stability of rock slopes when the rigid wedge slide type of failure is expected: Imperial College Rock Mechanics Research Reprints, 19, 10 pp (1972).

Stein, S., & Wysession, M. (2009). An introduction to seismology, earthquakes, and earth structure. John Wiley & Sons.

Tsai, V. C., Minchew, B., Lamb, M. P., & Ampuero, J. P. (2012). A physical model for seismic noise generation from sediment transport in rivers. Geophysical Research Letters, 39(2).

Werner, C., Wiesmann, A., Strozzi, T., and Wegmüller, U. (2008) "Gamma's portable radar interferometer," in Proc. 13th FIG Int. Symp. Deformation Meas. Anal./4th IAG Symp. Geodesy Geotech. Struct. Eng., 2008, pp. 1–10.

Werner, C., Wiesmann, A., Strozzi, T., Kos, A., Caduff, R., and Wegmüller, U. (2012) "The GPRI multi-mode differential interferometric radar for ground-based observations," in Proc. 9th EUSAR, 2012, pp. 304–307.

Wiesmann, A., Werner, C., Strozzi, T., and Wegmüller, U. (2008) "Measuring deformation and topogrphy with a portable radar interferometer," in Proc. 13th FIG Int. Symp. Deformation Meas. Anal./4th IAG Symp. Geodesy Geotech. Struct. Eng., 2008, pp. 1–9.

Wyllie, D.C., & Mah, C.W. (2004): Rock Slope Engineering. London: Spon Press (2004).

Yamada, M., Mangeney, A., Matsushi, Y., & Matsuzawa, T. (2018). Estimation of dynamic friction and movement history of large landslides. Landslides, 15(10), 1963-1974.

Zhu, L., & Rivera, L. A. (2002). A note on the dynamic and static displacements from a point source in multilayered media. Geophysical Journal International, 148(3), 619-627.

Tables and Figures

Table S1: Timeline of rock avalanche and debris flow observations as reconstructed from the debris flow early warning system at Prä (Figure 1) and eye witness reports (personal communication M. Keiser, Canton Grison).

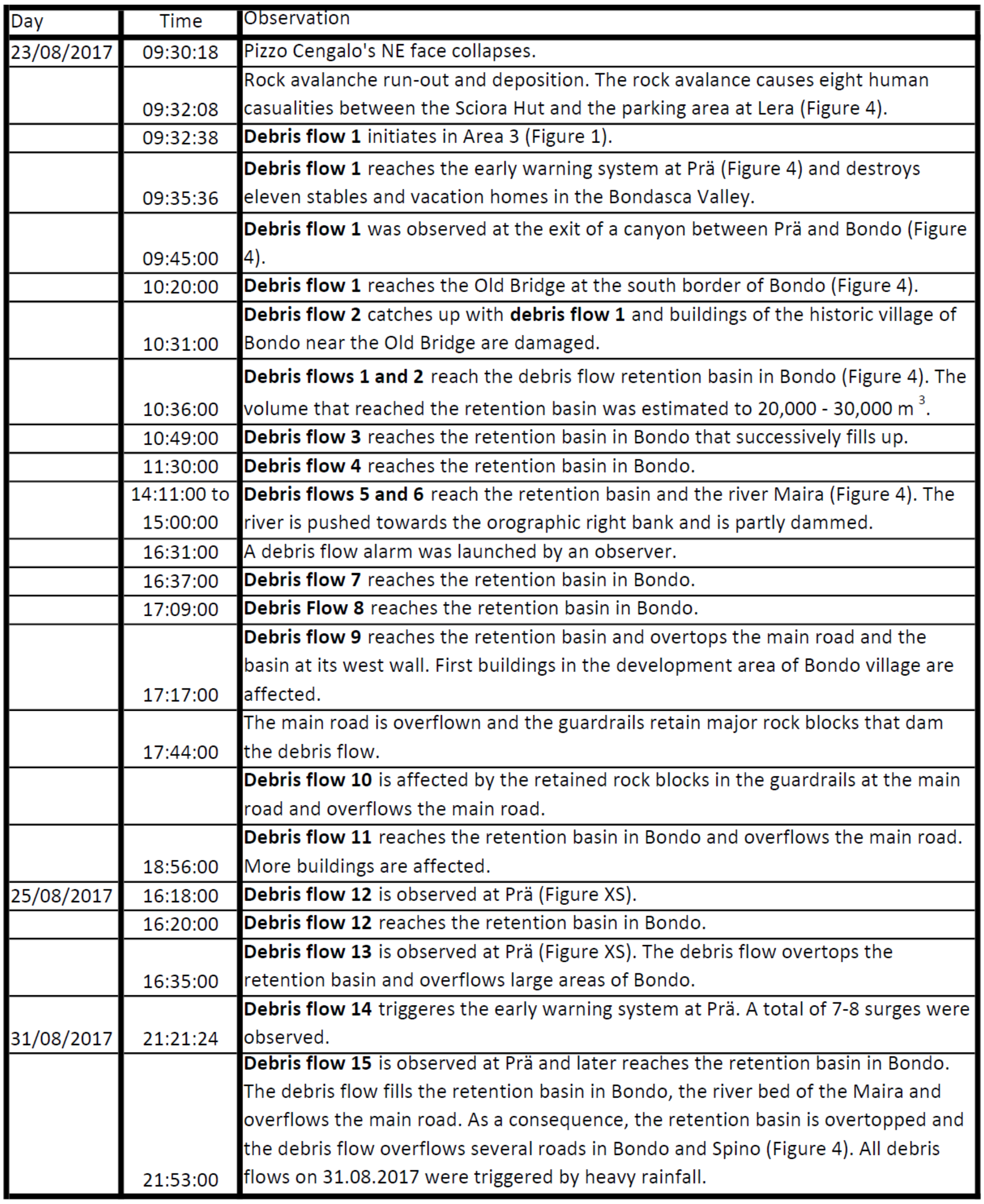

Day	Time	Observation
23/08/2017	09:30:18	Pizzo Cengalo's NE face collapses.
	09:32:08	Rock avalanche run-out and deposition. The rock avalance causes eight human casualities between the Sciora Hut and the parking area at Lera (Figure 4).
	09:32:38	**Debris flow 1** initiates in Area 3 (Figure 1).
	09:35:36	**Debris flow 1** reaches the early warning system at Prä (Figure 4) and destroys eleven stables and vacation homes in the Bondasca Valley.
	09:45:00	**Debris flow 1** was observed at the exit of a canyon between Prä and Bondo (Figure 4).
	10:20:00	**Debris flow 1** reaches the Old Bridge at the south border of Bondo (Figure 4).
	10:31:00	**Debris flow 2** catches up with **debris flow 1** and buildings of the historic village of Bondo near the Old Bridge are damaged.
	10:36:00	**Debris flows 1 and 2** reach the debris flow retention basin in Bondo (Figure 4). The volume that reached the retention basin was estimated to 20,000 - 30,000 m^3.
	10:49:00	**Debris flow 3** reaches the retention basin in Bondo that successively fills up.
	11:30:00	**Debris flow 4** reaches the retention basin in Bondo.
	14:11:00 to 15:00:00	**Debris flows 5 and 6** reach the retention basin and the river Maira (Figure 4). The river is pushed towards the orographic right bank and is partly dammed.
	16:31:00	A debris flow alarm was launched by an observer.
	16:37:00	**Debris flow 7** reaches the retention basin in Bondo.
	17:09:00	**Debris Flow 8** reaches the retention basin in Bondo.
	17:17:00	**Debris flow 9** reaches the retention basin and overtops the main road and the basin at its west wall. First buildings in the development area of Bondo village are affected.
	17:44:00	The main road is overflown and the guardrails retain major rock blocks that dam the debris flow.
		Debris flow 10 is affected by the retained rock blocks in the guardrails at the main road and overflows the main road.
	18:56:00	**Debris flow 11** reaches the retention basin in Bondo and overflows the main road. More buildings are affected.
25/08/2017	16:18:00	**Debris flow 12** is observed at Prä (Figure XS).
	16:20:00	**Debris flow 12** reaches the retention basin in Bondo.
	16:35:00	**Debris flow 13** is observed at Prä (Figure XS). The debris flow overtops the retention basin and overflows large areas of Bondo.
31/08/2017	21:21:24	**Debris flow 14** triggeres the early warning system at Prä. A total of 7-8 surges were observed.
	21:53:00	**Debris flow 15** is observed at Prä and later reaches the retention basin in Bondo. The debris flow fills the retention basin in Bondo, the river bed of the Maira and overflows the main road. As a consequence, the retention basin is overtopped and the debris flow overflows several roads in Bondo and Spino (Figure 4). All debris flows on 31.08.2017 were triggered by heavy rainfall.

Table S2: Seismic velocity model used for the inversion of the rock avalanche's force history.

Layer thickness (km)	P-velocity (km/s)	S-velocity (km/s)	Density (kg/dm^3)	Q_P	Q_S
3	5.6	3.237	2.14	225	100
7	5.98	3.457	2.56	225	100
10	6.02	3.48	2.87	225	100
10	6.57	3.798	3.00	225	100
5	7.63	4.41	3.00	225	100
10	7.81	4.5140	3.29	225	100
5	8.05	4.6530	3.29	225	100
200	8.15	4.711	3.29	225	100

Source: T. Diehl, N. Deichmann, S. Husen and E. Kissling. *Assessment of Quality and Consistency of S-Wave Arrivals in Local Earthquake Data*. EGU, Vienna, Austria, 2005.

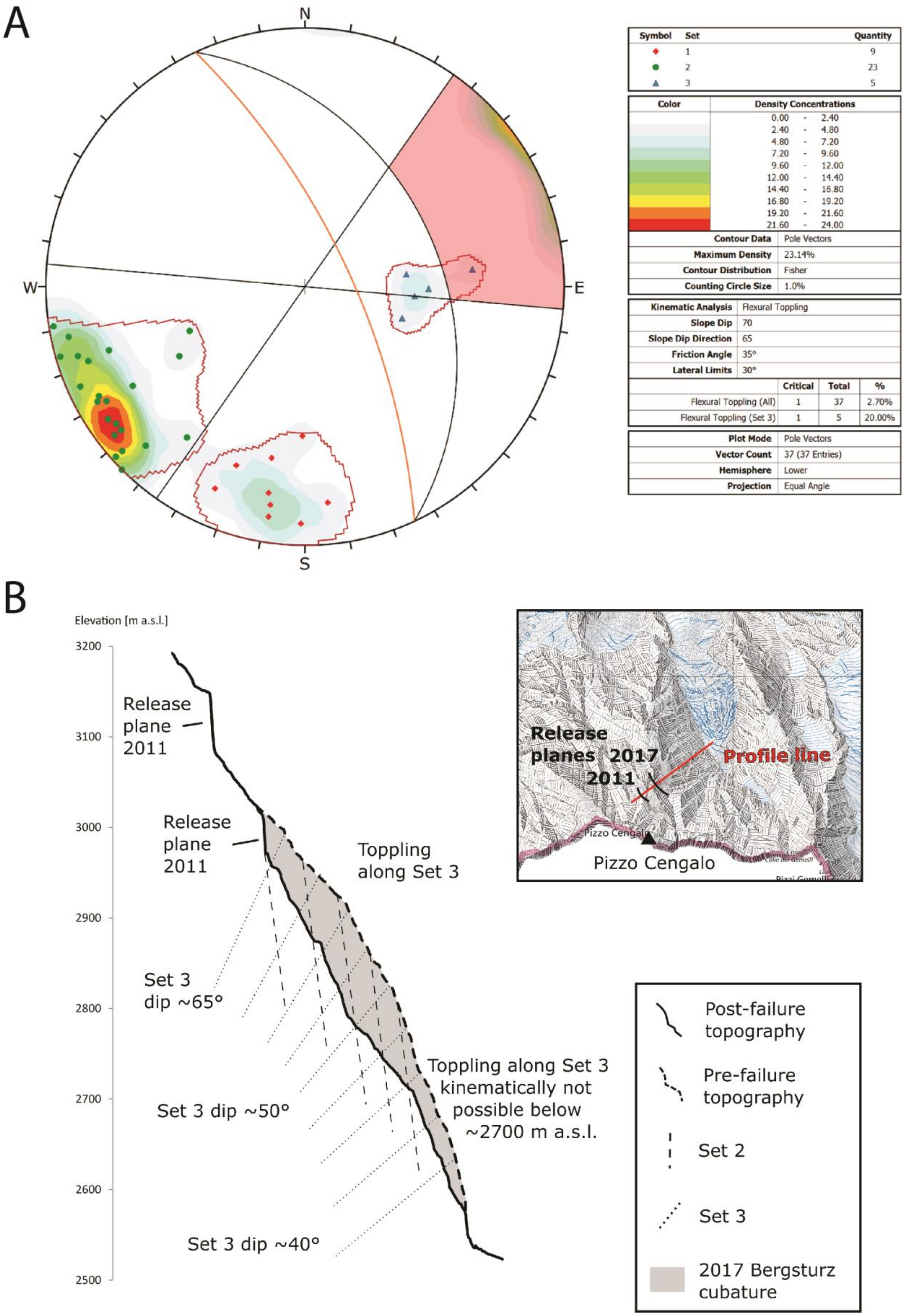
A
N
E
S
W
Symbol Set Quantity
♦ 1 9
● 2 23
▲ 3 5
Color Density Concentrations
0.00 - 2.40
2.40 - 4.80
4.80 - 7.20
7.20 - 9.60
9.60 - 12.00
12.00 - 14.40
14.40 - 16.80
16.80 - 19.20
19.20 - 21.60
21.60 - 24.00
Contour Data Pole Vectors
Maximum Density 23.14%
Contour Distribution Fisher
Counting Circle Size 1.0%
Kinematic Analysis Flexural Toppling
Slope Dip 70
Slope Dip Direction 65
Friction Angle 35°
Lateral Limits 30°
Critical Total %
Flexural Toppling (All) 1 37 2.70%
Flexural Toppling (Set 3) 1 5 20.00%
Plot Mode Pole Vectors
Vector Count 37 (37 Entries)
Hemisphere Lower
Projection Equal Angle
B
Elevation [m a.s.l.]
3200
3100
3000
2900
2800
2700
2600
2500
Release plane 2011
Release plane 2011
Toppling along Set 3
Set 3 dip ~65°
Set 3 dip ~50°
Toppling along Set 3 kinematically not possible below ~2700 m a.s.l.
Set 3 dip ~40°
Release planes 2017
2011
Profile line
Pizzo Cengalo
Pizzo Cengalo
Colle dei Gemelli
Pizzi Gemelli
Post-failure topography
Pre-failure topography
Set 2
Set 3
2017 Bergsturz cubature

Figure S1: Geological structures of the Piz Cengalo rock instability. (A) Stereographic projection of measurable joint sets in the Pizzo Cengalo NE wall. The joint set orientations were determined using terrestrial photogrammetric and terrestrial laser scanning data. Set 1 is approximately normal to the slope of the NE face (dip direction / dip = 005°/70°). Set 2 is slope parallel and dips steeply towards NE (065°/70°). Set 3 is conjugate to Set 2 and dips against the slope of the NE face. The dip angle of Set 3 decreases gradually from the top towards the toe of the NE face from 264°/66° to 263°/43°. (B) Cross-sectional sketch of geological structures.

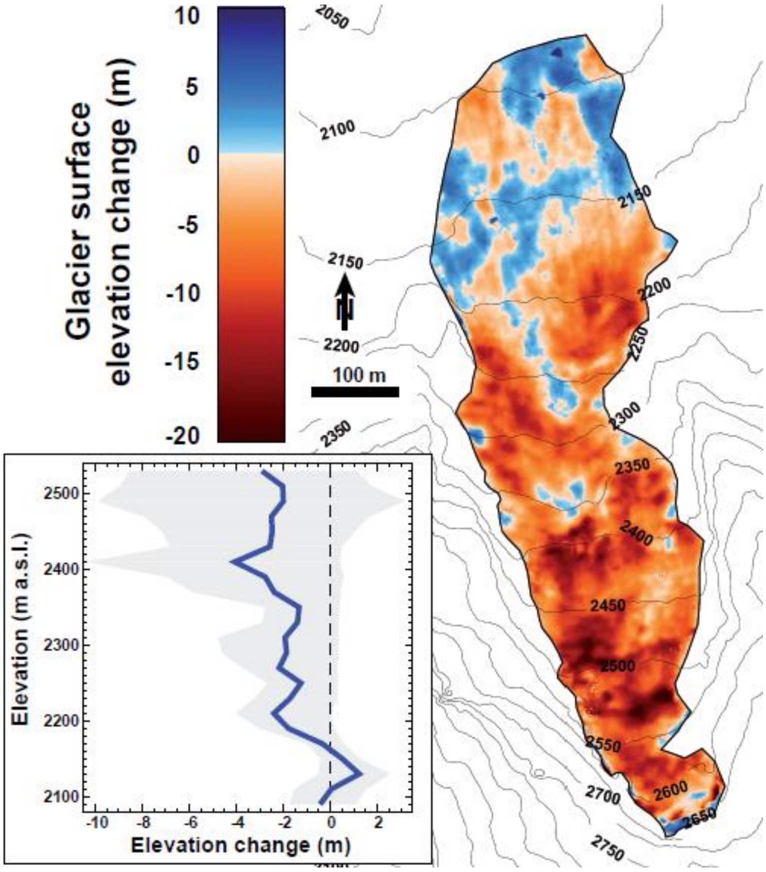

Figure S2: Ice surface elevation change of the small glacier at the foot of the Pizzo Cengalo rock face based on digital elevation models of 30 August 2015 and immediately after the 2017 failure. Elevation changes are only shown over the area covered by glacier ice before the event. Elevation changes are due to ice melt between 2015 and 2017, the direct erosional impact of the failure event and deposition of rock debris on the glacier surface. In the inset, average ice elevation changes are evaluated for elevation bins (blue: elevation bin average, grey shaded: spread of values).

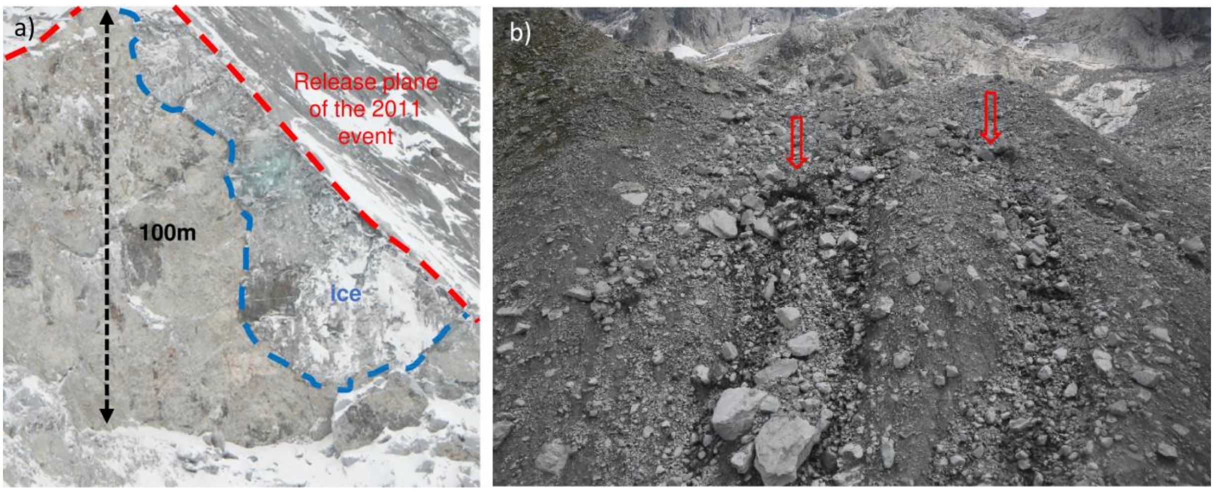

Figure S3: a) Rock fall release plane of the 2011 rock fall event. The right part of the release plane is covered with blue permafrost ice b) Blowholes in 2017 deposits in Area 1a (red arrows). Geyser-like water fountains were observed 25 to 40 minutes after the 2017 event from these blowholes.

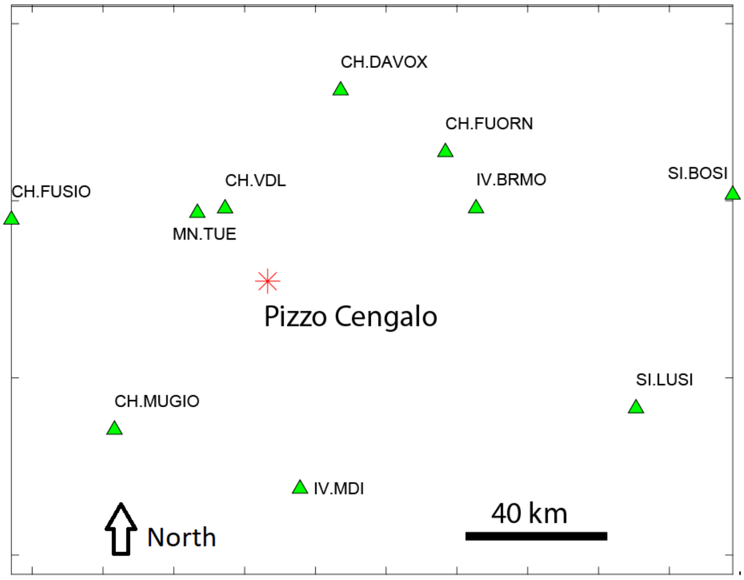

Figure S4: Map of seismic broadband stations near Pizzo Cengalo.

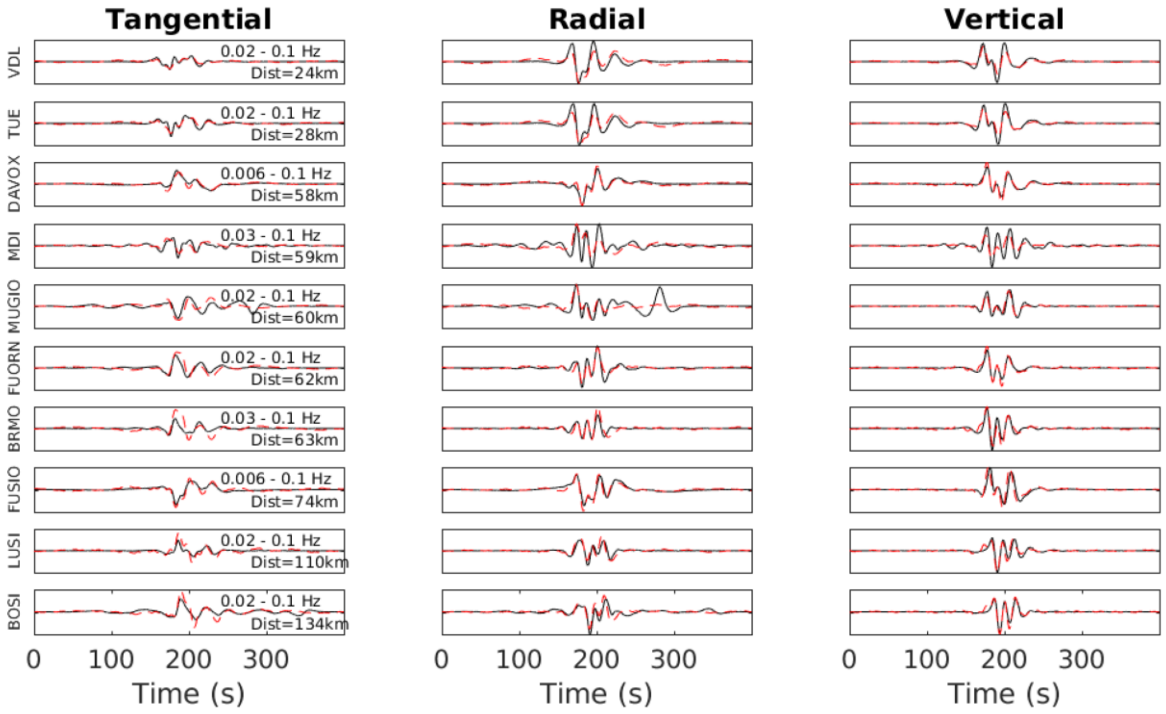

Figure S5: Three-component waveform fits (red dashed) to low-frequency seismic ground displacement records (black) of the 2017 Pizzo Cengalo rock avalanche. Station distances to rock avalanche and frequency ranges over which the inversion was applied and data were filtered, are indicated. Data and fits are normalized to the strongest component of a given station.

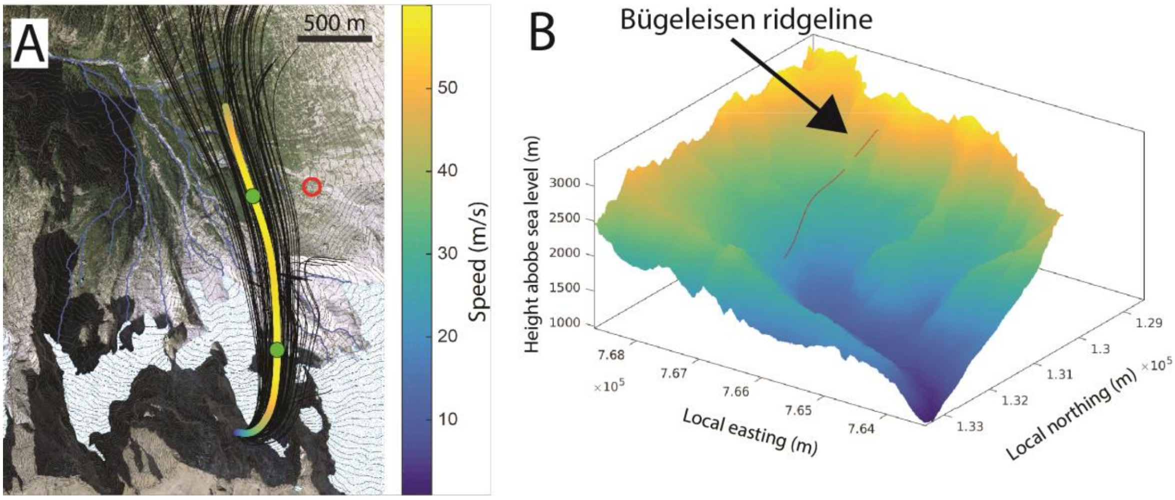

Figure S6: Rock avalanche trajectory. A: Same as Figure 7 of the main text, except for additionally showing all jackknife trajectories (black lines). B: Three dimensional view of the Bondasca Valley and the rock avalanche path (red) calculated from the mean of the jackknife force histories. Note that the terrain step (Figures 1 and 2 in the main text), which the rock avalanche encountered after more gently inclined terrain down-slope of the Bügeleisen ridgeline, manifests itself in the trajectory.

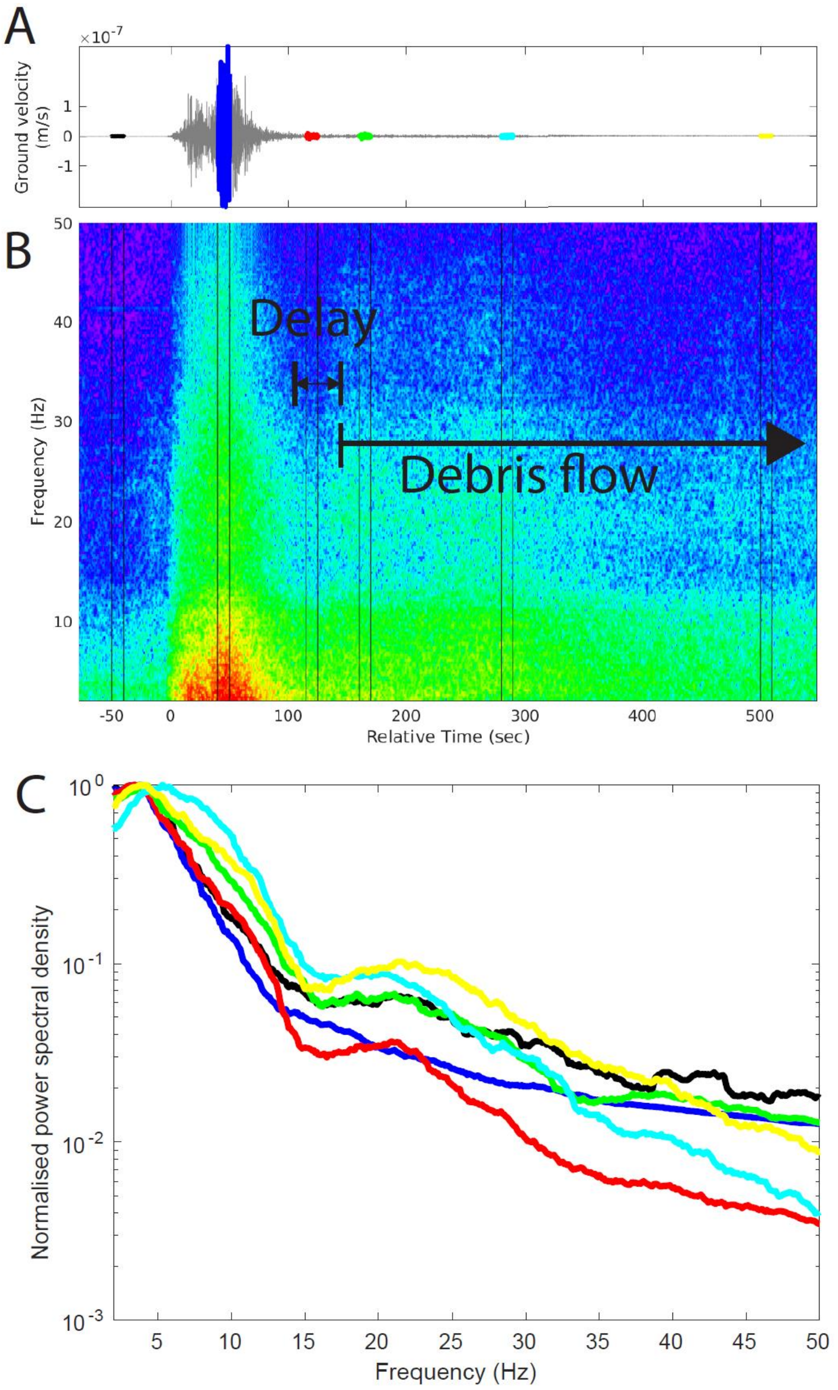

Figure S7: Spectral signature of the 2017 event. (A) time series with discussed sections color coded. (B) Spectrogram as in Figure 5 of the main text. Black vertical bars delimit the color coded seismogram sections in Panel (A). (C) Normalized spectra of the color coded seismogram sections in Panel (A).